PAPER

Check for updates

Microstructure, mechanical properties, and electrical conductivity of Mg−8Li−2Y−Zn/Al multilayered composites fabricated by cross asynchronous accumulative roll bonding

Hao Hu, [ab] Tongying Zhang,[a] Junli Wang [*b] and Jinsheng Li[a]

Mg−Li alloy is a material with great potential for development but its application in multiple fields is limited due to disadvantages, such as low strength and poor molding properties. In this study, Mg−8Li−2Y−Zn/Al multilayered composites were prepared by the Al layer cladding Mg−Li alloys using a cross asynchronous accumulative roll banding (CAARB) method, and the changes in microstructural characterization, mechanical properties, and electrical conductivity after rolling were evaluated. The results showed that the asynchronous rolling introduced additional shear variables, which provided the conditions for the aluminum layers to fracture to form wave patterns and improve the formability of the composites. The change in the rolling direction caused the grain orientation to be dispersed along the TD direction. The microhardness and tensile strength of the Mg−8Li−2Y−Zn/Al composites increased during the CAARB and reached a maximum after four cycles. In addition, calculations based on the skin depth indicate that the addition of Al layers benefits the composites in terms of improved electrical conductivity. Overall, the addition of Al layers allows more flexibility in the design and extension of Mg−Li alloys, and these findings provide insights into the control of microstructure and improvement of properties of Al/Mg−Li multilayered composites using the CAARB process.

1. Introduction

With the rapid development of aerospace, electronic technology, and other emerging industries, just using traditional single metals has been difficult to meet the needs of these industries for the comprehensive properties of materials. Therefore, layered metal composites have attracted extensive attention; they are combined with two or more metal plates through a specific preparation process, integrating the excellent properties of the component materials, and they become the new structural materials that can meet the performance requirements.[1–3] As the lightest metal structural materials as well as its advantages such as high specific stiffness and good electromagnetic shielding properties, magnesium alloys have great potential for development in aerospace and energy consumption in the automotive field.[4–6] However, the current magnesium alloys still have highlighted drawbacks, such as low strength and poor forming properties, which have a serious constraint on industrial application.[7] One of the common methods to increase the properties of magnesium alloys is to

use a surface protective layer. In this case, cladding a layer of aluminum on the surface of magnesium alloy causes flexibility in the design and expansion of magnesium alloy applications.[8] The purpose of Al/Mg composites is to use the advantages of Al and Mg metals and to strengthen the layered metal in applications that require both lightweight and high mechanical properties.[9–12]

In the previous study, it was found that using the conventional accumulative roll bonding (ARB) process can prepare materials with high strength and good elongation, it is also accompanied by microstructural inhomogeneity.[13,14] In recent years, Alizadeh[15] proposed an improved plastic deformation method named the cross accumulative roll bonding (CARB) process, which is based on the conventional ARB process, and first used this process to prepare Al/B$_4$C composites with more uniform second phase particle distribution and better tensile strength than the conventional ARB processing. Since then, researchers in various countries have used the CARB process to prepare a variety of metal-laminated composites with excellent properties, such as Cu/Zn/Al,[16] Al/Cu/Mn,[17] and Al/Zn.[18] Furthermore, in the study of rolling pressure for bimetallic rolling deformation, it was found that bimetals with relatively large layer thicknesses must be compounded under the condition of a large amount of depression, and it is difficult to compound in simultaneous cumulative stack rolling, while

[a]Faculty of Materials Science and Engineering, Kunming University of Science and Technology, Kunming 650093, China

[b]Research Center for Analysis and Measurement, Kunming University of Science and Technology, Kunming 650093, China. E-mail: 64291434@qq.com

asynchronous rolling can obtain larger deformation under the same rolling pressure to achieve the compounding of metals with relatively large layer thickness, so the researchers proposed an asynchronous accumulative roll bonding (AARB) process.[19,20] As such, the combination of the CARB process and the AARB process has become a new preparation method cross asynchronous accumulative roll bonding (CAARB) process, which is beneficial for improving the interface of the heterogeneous metal composite.

In this study, the CAARB process was used to prepare Mg–8Li–2Y–Zn/Al multilayered composites. The effects of CAARB process parameters, such as cycles, on microstructural characterization and mechanical properties, were also investigated, and the influencing factors of electrical conductivity and the phase complementation effect played by Al layers were studied, which provided theoretical guidance and experimental basis for the new composites.

2. Experimental section

2.1. Materials and preparation

In this experiment, Mg–8Li–2Y–Zn alloy and Al (purity: 99.9 wt%) were used as raw materials. Table 1 demonstrates the chemical composition of Mg–8Li–2Y–Zn alloy, and its thickness was 1 mm, and the thickness of industrial pure aluminum grade 1070 was 0.015 mm.

The schematic of the CAARB process and extruded specimens are displayed in Fig. 1. From Fig. 1a, Mg–8Li–2Y–Zn/Al multilayered composites were fabricated in two steps. The first step was the original Mg–8Li–2Y–Zn alloy preparation process, in which specimens were cut into $50 \times 30 \times 1$ mm^3 size. Firstly, the original sheet was fully clad with double gloss aluminum foil, and the clad sheet was preheated before in

a holding tank at 350 °C for 5 min, after which, it was rolled on a two-roller asynchronous mill (the asynchronous ratio is 1 : 1.08) with the reduction of 50%. One cycle plate was rolled for surface treatment, and then cut into two thin plates of the same size along the RD direction in the second step, two plates were simultaneously rotated 90° clockwise around the ND direction. After that, the layers were stacked on each other with a sequence of Al/Mg alloy/Al/Mg alloy/Al. As shown in Fig. 1b, the specimens with different CAARB cycles were designated CAARB0, CAARB1, CAARB2, CAARB3, and CAARB4, respectively.

2.2. Morphology observation and XRD

The microstructural observation was performed using optical microscopy (LEICA DM2500 M, OM) and scanning electron microscopy (ESCAN VEGA II LMU, SEM) equipped with an energy dispersive spectrometer (EDS) to observe the microstructure evolution of the Mg layer on the RD–ND section, as shown in Fig. 1c. The thickness of the intermetallic layers and grain size were measured using the ImageJ software. The phase composition was studied using X-ray diffraction (D/max-2200, XRD). The data were collected with a scanning rate of 1° min^{-1} by using CuKα radiation at 30 kV.

2.3. Measurements of mechanical properties

The microhardness tests were carried out on the HSX-1000A detector, 8 points were taken for each α-Mg phase and β-Li phase, and the average values were calculated. Tensile tests were performed at room temperature on the SHIMADZU SLFL-100KN testing equipment with a tensile speed of 1.7 mm min^{-1}. The sampling position was the middle part of the rolled alloy, selected to eliminate the impact of defects on the side parts on the accuracy of the experiment. The tensile specimens were immediately photographed with fracture scanning to avoid fracture oxidation.

2.4. Measurements of electrical conductivity

The conductivity measurement method used in this study was the eddy current conductivity method, which was performed on

Table 1 Chemical composition of Mg–8Li–2Y–Zn magnesium alloy (wt%)

Element	Li	Y	Zn	Mn	Fe	Mg
Content	7.86	1.98	0.97	0.023	0.0034	Bal.
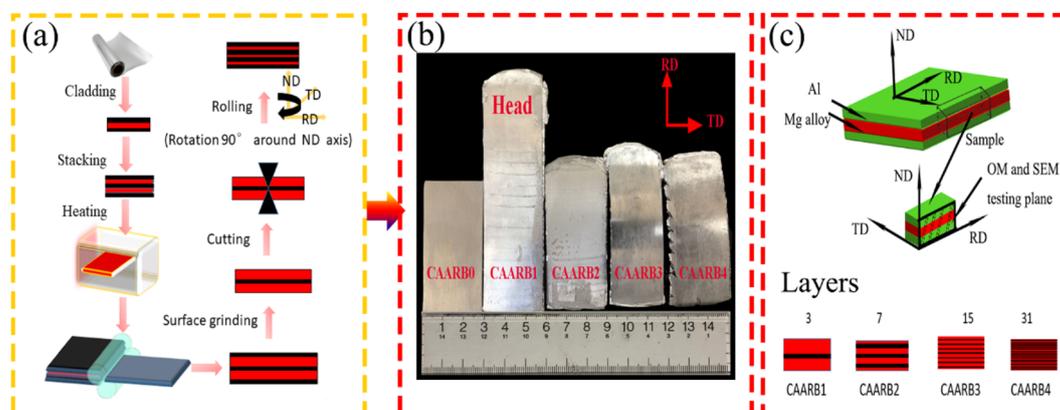
Fig. 1 Schematic of fabrication and specimens: (a) preparation process of CAARB0 to CAARB2; (b) specimens; (c) sampling locations of different CAARB cycles.

an eddy current conductivity meter model 7501 manufactured by Xiamen Second Electronic Instrument Factory. The electrical conductivity test of the material requires a certain flatness of the surface, therefore, the samples must be ground with 100 #, 200 #, 500 #, and 1000 # sandpaper. In the testing process, to ensure the accuracy of the measurement data, 10 test points were selected for each sample along the RD direction, and the distance between each two test points was 0.5 mm, and the average value was taken as the conductivity value of the specimens.

3.   Results and discussion

3.1.   Microstructural characterization

The changes in the interfacial bonding morphology of the Mg–8Li–2Y–Zn/Al multilayered composites during the CAARB process are shown in Fig. 2. From Fig. 2a–d, the OM observation shows tight bonding between the Mg alloy and Al layers under the CAARB processing. In the subsequent cycles, the bonding of the interface introduced in the previous cycle was improved, and the presence of the interface was almost invisible at 1/4 of the CAARB4. The thickness of both Mg alloy and Al layers gradually decreased with the accumulated amount of deformation. Due to the difference in rheological stress, thickness, and the hardness between the heterogeneous metals, the deformation of the hard phase material is small and the deformation of the soft phase is large, and this uneven deformation will lead to the destabilization of the hard phase layer firstly during the CAARB processing, the hard phase layers initially yield a distinct wave pattern until necking.

Fig. 3 shows the SEM image and EDS analysis of CAARB4. From the area scan, it is obvious to observe that the Al layers are severely thinned after 4 cycles, and due to the stress concentration at the necking, the continued deformation will cause the phase at the necking to elongate and rupture, and be wrapped up by the magnesium matrix and distributed diffusely in the material, which will provide the metallurgical bonding interface space to achieve the bonding between the two Mg layers;

correspondingly, there were no bonding defects in the interface, according to the line scan results, forming the metallurgical bonding structure composed of the Al–Mg inter-diffusion zone.

Fig. 4 shows the SEM-EDS image and XRD pattern of the Mg–8Li–2Y–Zn/Al multilayered composites. According to the binary phase diagram of the Mg–Li alloys and the literature,[21,22] the dual-phase alloy is mainly composed of a white α-Mg phase and a gray β-Li phase. From Fig. 4a, there are some bright white particles in the alloy, and these bright white particles are mainly distributed in the β-Li interior or at the boundary of the α/β phases. To determine the elemental composition of the second phase in Mg–8Li–Y–Zn alloy, area scanning and A-point scanning were carried out. The results show that the mass ratio of the bright white particles in Mg–8Li–Y–Zn alloy is Mg : Y : Zn = 68.2 : 19.4 : 12.4. According to the relative atomic mass of Mg, Y, and Zn, the atomic number ratio in the chemical formula of the bright white particles can be calculated as 12 : 1 : 1. As can be seen from Fig. 4b, the diffraction peaks of α-Mg, β-Li, and $Mg_{12}YZn$ can be observed. Therefore, the bright white particles in the microstructure are considered as having the $Mg_{12}YZn$ phase. The XRD patterns of the samples under different cycles are shown in Fig. 4c. After the CAARB process, there is no phase transformation, and it is not difficult to find that the (0002) crystal surface peak of α-Mg has not changed significantly. It indicates that the CAARB process has a weakening effect on the surface texture, due to the different linear velocities of the upper and lower roll surface, in addition to the positive pressure caused by rolling, there is also parallel to the rolling direction shear stress, which in turn weakens the conventional rolling to the Mg alloy produced by the (0002) basal texture as the dominant plate texture.

Fig. 5 indicates the microstructure and grain size of the Mg alloy layers in the Mg–8Li–2Y–Zn/Al composites on the RD–ND and RD–TD planes under different CAARB cycles. As revealed in Fig. 5a–i, in CAARB1, the irregularly-arranged α-Mg and β-Li in the alloy underwent elongation deformation, and the grain size of α-Mg decreased to 2.84 μm in the ND direction. Equally, due to the non-uniformity of polycrystalline plastic deformation, it
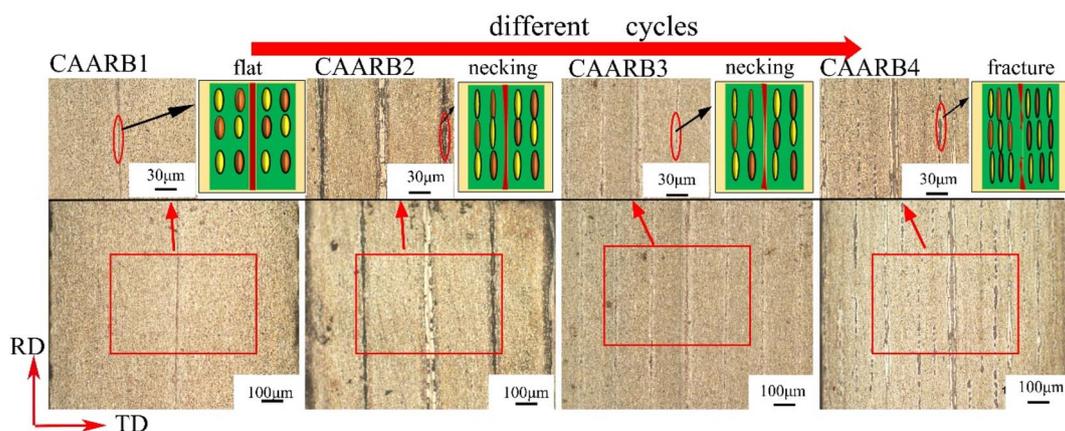

Fig. 2 Interface combination Mg−8Li−2Y−Zn/Al multilayered composites by CAARB processing: (a) CAARB1; (b) CAARB2; (c) CAARB3; (d) CAARB4.
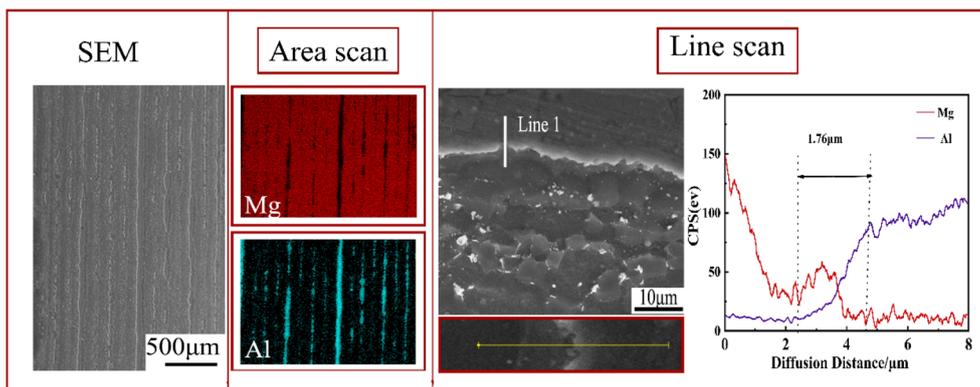
Fig. 3 SEM image and EDS analysis of CAARB4.

can be seen that the α-Mg phase deformation ratio is larger because the α-Mg phase is an HCP structure, which cannot enter plastic deformation at the same time. There is not enough shear stress to make it slip, in this way, the hard α-Mg phase

hinders the deformation of the soft β-Li phase. In CAARB2, due to the change in the rolling direction, the directionality in the fibrous tissue along the RD direction is weakened and there is a tendency to disperse along the ND direction. Some lamellar α-
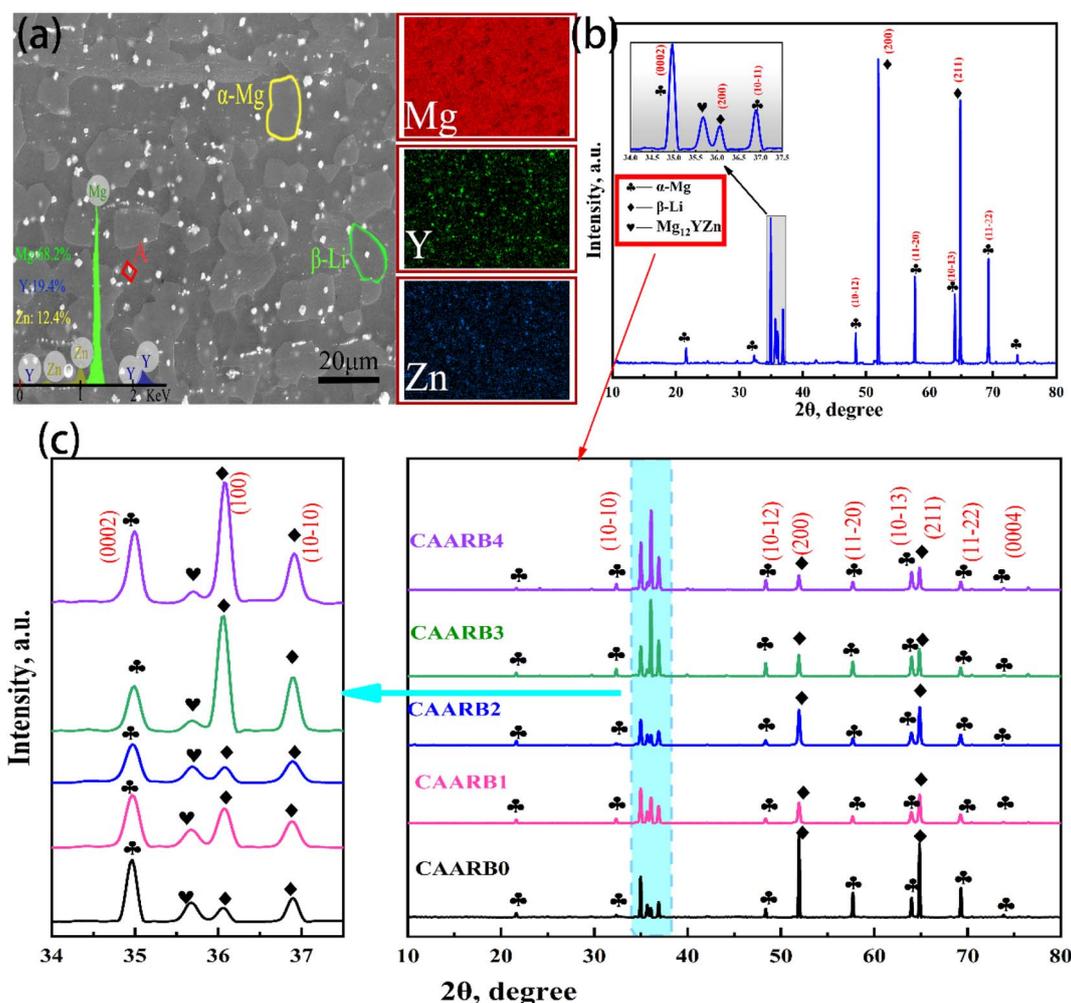

Fig. 4 SEM-EDS image and XRD pattern of the Mg–8Li–2Y–Zn/Al multilayered composites: (a) SEM-EDS image of original status; (b) XRD pattern of original status; (c) XRD patterns of the samples under different cycles.
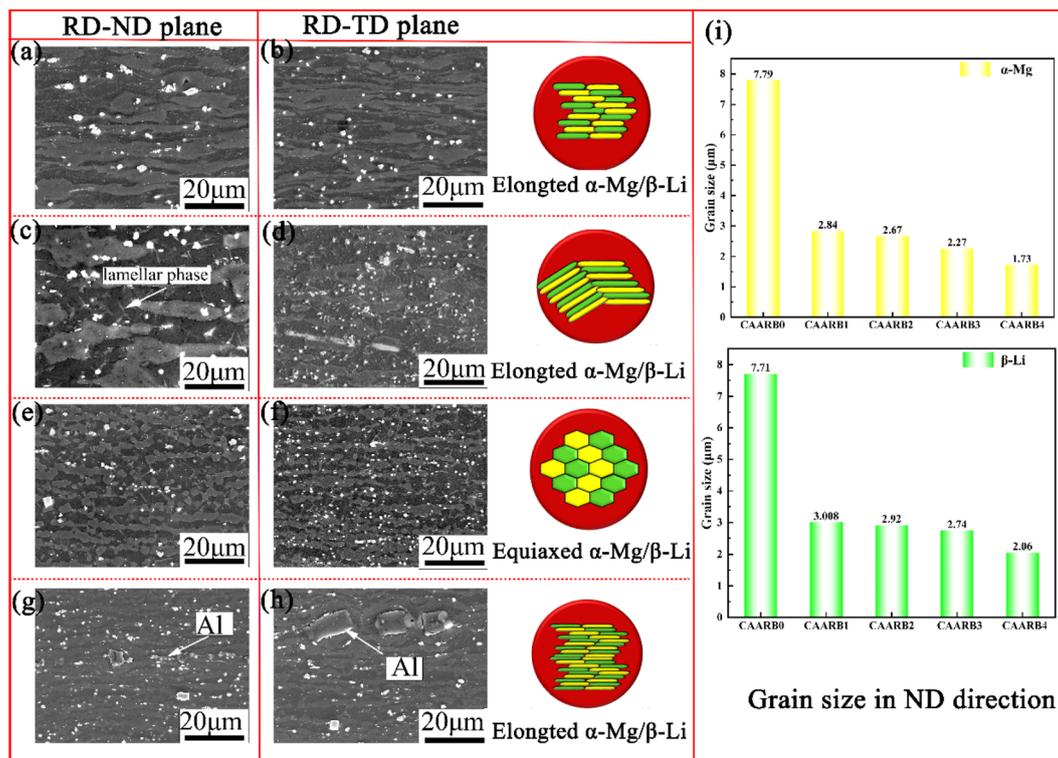
Fig. 5 Microstructure and grain size of Mg−8Li−2Y−Zn/Al multilayered composites under different cycles: (a and b) CAARB1; (c and d) CAARB2; (e and f) CAARB3; (g and h) CAARB4; (a, c, e, and g) on the longitudinal section (the RD−ND plane); (b, d, f, and h) on the cross-sectional views (RD−TD plane); (i) grain size in the ND direction.

Mg formation was observed in the RD–ND plane and RD–TD plane, which indicates that the grains are deflected along the specific grain planes. The α phase accumulates stress internally with the increase in deformation, and further fragmentation and uniform dispersion into the α-Mg phase occur during the CAARB3, the tissue distribution is more uniform and the

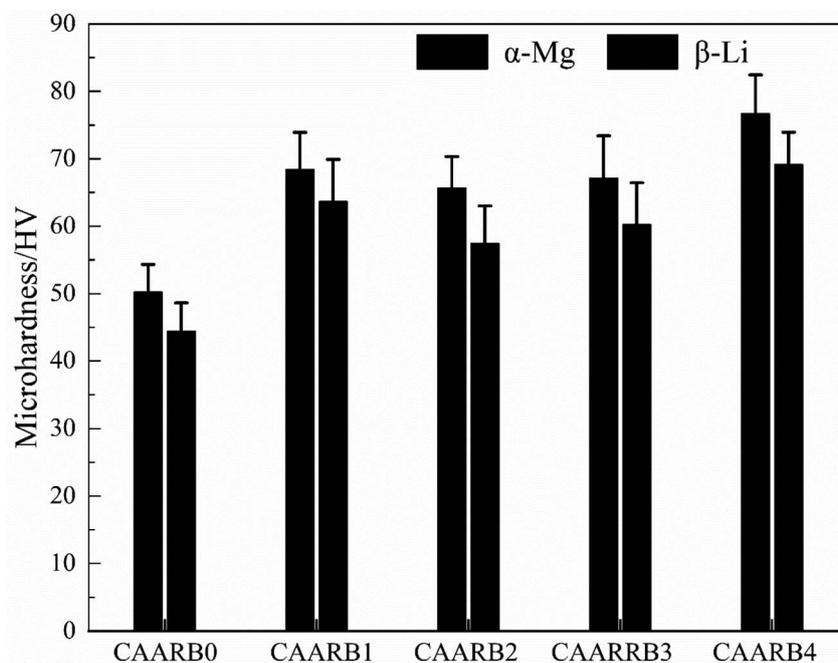**Fig. 6** Microhardness of Mg−8Li−2Y−Zn/Al composites with different cycles.
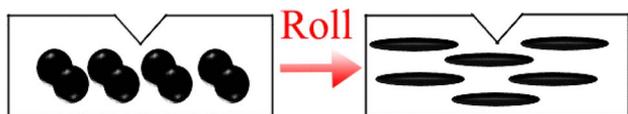
Fig. 7 The mechanism of microhardness.

number of large-sized grains is reduced. The RD–TD plane behaves more significantly than the RD–ND plane. In CAARB4, a large amount of strain was accumulated, which led to sufficient grain refinement, and the grain size of α-Mg was refined to 1.73 μm in the ND direction at this time. It can be found that the Al layer fractured in both the RD–ND and RD–TD planes. Additionally, it can also be observed that $Mg_{12}YZn$ was continuously broken into finer dispersed small dot-like particles with deformation during CAARB processing, and was evenly distributed in the matrix.

3.2. Mechanical properties

3.2.1. Microhardness. The microhardness of the Mg–8Li–2Y–Zn/Al multilayered composites under different CAARB process cycles is shown in Fig. 6. In CAARB2, the degree of grain refinement was accompanied by a small increase in the number of dislocations in the alloy due to the change in the rolling direction. In CAARB3, the dynamic deformation energy storage as the driving force at this stage induced the generation of the dynamic recrystallization phenomenon of α-Mg grains and β-Li grains in the alloy, which to some extent reduces the internal

part of the deformation energy storage in the alloy, so the microhardness was increased not obvious enough, while at CAARB4, the dislocation density had reached the maximum in all directions to improve the microhardness value. In addition, the microhardness of the α-Mg phase is higher than that of the β-Li phase on each cycle, indicating that in terms of microhardness performance, the α-Mg phase behaves as a hard phase, the β-Li phase behaves as a soft phase, and the changing trend of the two phases remains the same in the whole. This indicates that both of them changed together in a coordinated manner under large plastic deformation. Fig. 7 represents the mechanism of microhardness. The finer the grain size after rolling, the less favorable it is for the crack extension, which increases the microhardness, therefore, the microhardness of the composites has increased compared to CAARB0.

3.2.2. Tensile properties. The tensile property curves under different CAARB cycles are shown in Fig. 8. From Fig. 8a, it can be seen that the tensile strength of Mg–8Li–2Y–Zn/Al composites was significantly improved under the CAARB process, and the tensile strength increased dramatically from 171.12 MPa to 249.17 MPa after 4 cycles, and the elongation decreased from 25.06% to 6.42%. As shown in Fig. 8b, where no fracture occurred immediately after reaching the maximum stress value before 3 cycles, indicating that the whole deformation process proceeded very uniformly. The work hardening rate curves represented in Fig. 8c clearly show that in stage II (the stage where the strain hardening rate decreases sharply in a linear trend), there is a great difference before and after deformation,
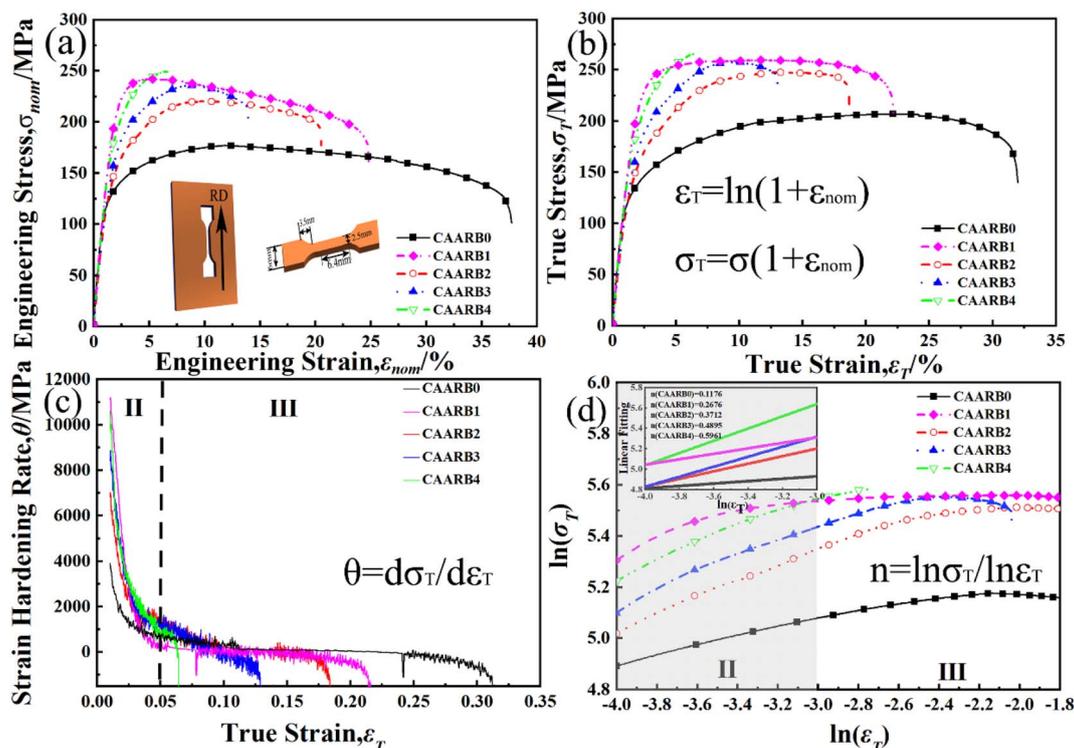

Fig. 8 The tensile properties of Mg–8Li–2Y–Zn/Al multilayered composites with different cycles: (a) engineering stress and strain; (b) true stress and strain; (c) strain hardening rate; (d) hardening index.

Table 2 Mechanical properties of Mg–8Li–2Y–Zn/Al composites with different CAARB cycles

Cycles	UTS (MPa)	ε_{nom}	α-Mg (HV)	β-Li (HV)
CAARB0	171.12	25.06%	50.23 ± 4.1	44.41 ± 4.2
CAARB1	241.70	16.51%	68.41 ± 5.5	63.62 ± 6.3
CAARB2	227.25	14.15%	65.62 ± 4.7	57.40 ± 5.6
CAARB3	236.83	7.88%	67.10 ± 6.3	60.23 ± 6.2
CAARB4	249.17	5.42%	76.72 ± 5.7	69.13 ± 4.8

which is related to the degree of dislocation plugging inside the material. Combined with the consideration that the θ value of the alloy is always higher than the initial state before the material yielding occurs, it indicates that the Mg–8Li–2Y–Zn/Al composites have completed the rapid accumulation of dislocations in the early stage of plastic deformation. To further explore the work-hardening behavior of the alloy under different passes, the work-hardening indices of the magnesium alloy under different passes are examined here, and the linear fitting analysis is carried out for the work-hardening stage II. The results are shown in Fig. 8d, in stage II, the n value increases with an increase in the deformation degree, which is mainly due to the change of rolling direction between CAARB cycles so that the force on the plate is no longer concentrated in one area. The dislocations along the RD direction formed in the previous passes are dispersed and the distribution position is increased, and the dislocation density in all directions of the sheet reaches maximum when CAARB is carried out to 4 cycles. This results in a significant process-hardening effect, which leads to a larger n value. Materials with a large n value have a high strain-hardening effect and improved interfacial bonding, which is less likely to produce cracks. A comprehensive consideration is given to the trends in strength and elongation changes, which are due to the combined effects of the fine grain strengthening effect and the improvement of the bonding effect between metal layers. The finer the grain, the greater the resistance of grain boundaries to the slip of dislocations, the greater the difficulty of coordinated deformation, and the higher the strength of the metal. The severe plastic deformation case leads to the generation of the work hardening phenomenon, and then the specimen tensile strength increases and plasticity decreases. After CAARB3, the interlayer interfaces partially disappeared, and Mg/Al formed a high-density phase interface. The slip of dislocations is strongly restrained by the high-density phase interfaces. As a consequence, the strength continues to increase, whereas the elongation to failure begins to decrease.

Table 2 shows the mechanical properties under different CAARB cycles. It can be seen more intuitively that the mechanical properties of the multilayer material are significantly improved with the increase in the number of asynchronous cumulative stacking. After four passes, the microhardness increased by 44.7%, and the tensile strength increased by 45.5%. In conclusion, the mechanical properties of the material can be significantly improved by the CAARB process.

Fig. 9 shows the fracture morphology of the Mg–8Li–2Y–Zn/Al multilayered composites. It can be seen that there are more equiaxed dimples in the tensile fracture from CAARB0 to CAARB2, so the elongation of the sheets is maintained in a stable range and the fracture form is mainly a ductile fracture. However, after the CAARB process, it is obvious that the number of dimples becomes less, and the large tearing dimples consist of lamellar dimple structures, and it is further observed that there are many small particles distributed inside the part of the dimples, which were analyzed to be the particles of intermetallic compounds after breaking. In CAARB3 and CAARB4, from the facet to facet connection by the tearing ridges, the tearing ribs contained deconstruction steps, and their morphology showed
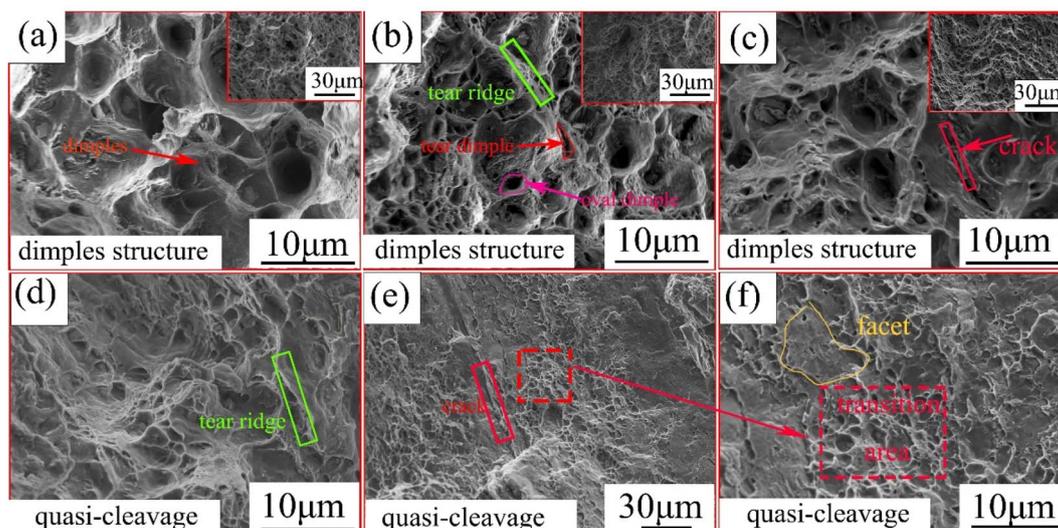
Fig. 9 Fracture morphology of the Mg–8Li–2Y–Zn/Al composites: (a) CAARB0; (b) CAARB1; (c) CAARB2; (d) CAARB3; (e and f) CAARB4.
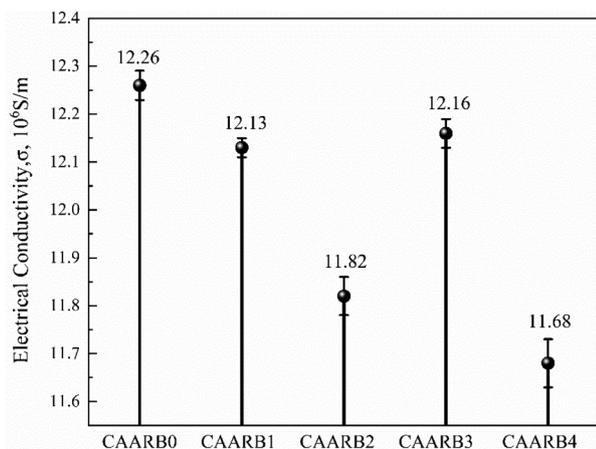
Fig. 10 Electrical conductivity of specimens at different CAARB cycles.

Table 3 The skin depth of Mg–8Li–2Y–Zn/Al composites of different CAARB cycles

Samples	The thickness of single Mg layer (mm)	Skin depth (mm)
CAARB1	0.5140	0.2045
CAARB2	0.2594	0.2071
CAARB3	0.1228	0.2042
CAARB4	0.0588	0.2084

a quasi-cleavage fracture, which indicated a decrease in elongation, the characteristics of these fractures are consistent with the increase in elongation in the tensile curve.

3.3. Electrical conductivity

The electrical conductivity is measured using the eddy current conductivity meter, this measurement instrument calculates the electrical conductivity of the material by the force of the vortex-like current induced on the surface and near-surface of the material, and the eddy current only exists in the near-surface of the material within the skinning depth of the material, and the calculation of the skinning depth is shown in eqn (1).[23]

$$\delta_s = \frac{1}{\sqrt{\pi \mu_0 \mu_r f \sigma}} \quad (1)$$

The operating frequency f of the experimental eddy current conductivity instrument is 500 kHz, and the magnesium alloy is a non-magnetic material, its permeability $\mu = \mu_0 = 4\pi \times 10^{-7}$ N A^{-2} (μ_0 is the vacuum permeability), the relative permeability μ_r is 1, and by inserting the electrical conductivity from Fig. 10 into the formula, the material's skinning depth can be calculated. The results of the calculations, combined with the thickness of the monolayer of Mg–8Li–2Y–Zn/Al composites of different CAARB cycles, are shown in Table 3.

The skinning depth is less than the thickness of the monolayer of Mg–8Li–2Y–Zn alloy for CAARB1 to CAARB2, and the measured value of conductivity is Mg alloy at this time, while the measured value of conductivity is Mg–8Li–2Y–Zn alloy and Al layers partially diffused in the matrix for CAARB3 and CAARB4. It can be seen that the conductivity of the material decreases with the number of rolling passes, but in CAARB3, the electrical conductivity reversion occurs. Generally for metallic materials, the conductivity of the material is closely related to the material organization, specifically, the smaller the grain size, the more serious the scattering phenomenon of the electrons, and the worse the conductivity of the material (except for nanocrystals); and the higher the internal density of the material, the more serious the scattering phenomenon of the electrons to the material, the lower the conductivity of the material. In CAARB1 and CAARB2, as the materials have accumulated a large number of strains, the dislocation density of the alloy keeps increasing due to the accumulation of deformation energy storage, so the conductivity of the material decreases. In CAARB3, the deformation energy in the alloy decreases, and the presence of some Al layers can make the conductivity of the alloy recover, but in CAARB3, the conductivity is still lower than in CAARB0 because there is still some deformation energy in the alloy. In CAARB4, the deformation energy accumulation of the material is the largest, so the conductivity is the lowest.

The processing conditions and properties of Mg/Al multilayered composites are presented in Table 4. Achieving high ultimate tensile strength and high elongation in Mg/Al multilayered composites under conditions has been quite difficult, however, the CAARB process to prepare Mg/Al multilayered composites performed well in this work and were significantly higher than most of the reported composites. In addition, the electrical conductivity of Mg/Al multilayered composites has rarely been reported. In this work, experiments coupled with theoretical calculations were performed to evaluate the

Table 4 Comparison between the properties obtained in this study with those of other multilayered composites

Materials	Process-cycle-temperature (°C)	UTS (MPa)	Elongation (%)	Microhardness (HV)	References
Al (1060)/Mg (Mg–8Li–2Y–Zn)	CAARB-1 cycle-room	241	16.5	69	Present study
Al (1050)/Mg (AZ31)	ARB-1 cycle-room	177	7.8	72	24
Al (1060)/Mg (Mg–0.2Al–1.75Mn–0.75Ce)	Roll cladding-1 cycle-200	150	0.8	45	25
Mg–Li–Al/Al–Li	ARB-2 cycle-room	217	13	62	26
Al (1050)/Mg (pure Mg)	ARB-1 cycle-room	253	4.5	72	27
Al (1050)/Mg (LZ91)	ARB-1 cycle-room	174.7	13.6	—	28
Al (1050)/Mg (pure Mg)	ARB-1 cycle-room	190	5.9	—	29
Al (1050)/Mg (AZ31)	AARB-1 cycle-room	107	—	46	30

electrical conductivity of Mg/Al multilayered composites, expanding the application potential of Mg/Al multilayered composites.

4. Conclusion

Mg–8Li–2Y–Zn/Al multilayered composites were successfully fabricated by the CAARB process. In addition to improving the sample edge cracking situation, it also showed excellent mechanical properties, with a microhardness of 72.93 HV and ultimate tensile strength of 249.17 MPa in CAARB4. Meanwhile, for electrical conductivity, the introduction of the Al layer into the calculation of skin depth expanded the application of multilayer composites, and the organization of multilayer composites became more uniform by adjusting the orientation of rolling. In the future, exploring the composites with a reasonable number of layers and layer thickness ratio parameters for the best forming performance is the key to the development and application of Mg/Al multilayered composites.

Author contributions

Hao Hu: investigation, methodology, data curation, writing – original draft, writing – review and editing. Tongying Zhang: investigation, writing – review and editing. Junli Wang: conceptualization, resources, supervision, writing – review and editing, funding acquisition. Jinsheng Li: data curation, writing – review and editing.

Conflicts of interest

There are no conflicts to declare.

Acknowledgements

References

1 Y. Wang and K. S. Vecchio, Microstructure evolution in Fe-based-aluminide metallic–intermetallic laminate (MIL) composites, *Mater. Sci. Eng., A*, 2016, **649**, 325–337, DOI: **10.1016/j.msea.2015.10.019**.

2 Y. M. Zhang, H. J. Zhao, B. H. Deng, S. Basu, L. P. Huang and Y. F. Shi, Design Ductile and Work-Hardenable Composites with All Brittle Constituents, *Acta Mater.*, 2021, **208**, 116770, DOI: **10.1016/j.actamat.2021.116770**.

3 Z. G. Liu, X. H. Gao, M. Xiong, P. Li, R. D. K. Misra, D. Y. Rao and Y. C. Wang, Role of hot rolling procedure and solution treatment process on microstructure, strength and cryogenic toughness of high manganese austenitic steel, *Mater. Sci. Eng., A*, 2021, **807**, 140881, DOI: **10.1016/j.msea.2021.140881**.

4 J. W. Feng, H. Zhang, L. Zhang, G. D. Zou, J. Wang and Q. M. Peng, Microstructure and corrosion properties for ultrahigh-pressure Mg–Li alloys, *Corros. Sci.*, 2022, **206**, 110519, DOI: **10.1016/j.corsci.2022.110519**.

5 Z. X. Kang, K. Lin and J. Y. Zhang, Characterisation of Mg–Li alloy processed by solution treatment and large strain rolling, *Mater. Sci. Technol.*, 2015, **32**(5), 498–506, DOI: **10.1179/1743284715Y.0000000119**.

6 W. L. Wang, L. He, X. Yang and D. Wang, Microstructure and microhardness mechanism of selective laser melting Mg–Y–Sm–Zn–Zr Alloy, *J. Alloys Compd.*, 2021, **868**, 159107, DOI: **10.1016/j.jallcom.2021.159107**.

7 S. Jana, M. Olszta, D. Edwards, M. Engelhard, A. Samanta, H. T. Ding, O. B. Lsgor and A. Rohatgi, Microstructural Basis for Improved Corrosion Resistance of Laser Surface Processed AZ31 Mg Alloy, *Corros. Sci.*, 2021, **191**, 109707, DOI: **10.1016/j.corsci.2021.109707**.

8 Y. Z. Liu, Y. J. Bai, J. T. Chen, H. Chen, Z. T. Zhu and Y. X. Li, Control of intermetallic compounds in Ultrasonic-Assisted Sn soldering of Mg/Al alloys, *Mater. Des.*, 2022, **223**, 111235, DOI: **10.1016/j.matdes.2022.111235**.

9 J. L. Wang, F. Guan, W. M Jiang, G. Y. Li, Z. Zhang and Z. T. Fan, The role of vibration time in interfacial microstructure and mechanical properties of Al/Mg bimetallic composites produced by a novel compound casting, *J. Mater. Res. Technol.*, 2021, **15**, 3867–3879, DOI: **10.1016/j.jmrt.2021.10.037**.

10 X. L. Bi, Y. J. Hu, H. J. Zhao and T. B. Li, A novel method for preparing Al/Mg/Al laminated composite material, processing maps and interface diffusion analysis, *J. Alloys Compd.*, 2021, **900**, 163417, DOI: **10.1016/j.jallcom.2021.163417**.

11 D. Rahmatabadi, M. Pahlavani, M. D. Gholami, J. Marzbanrad and R. Hashemi, Production of Al/Mg–Li composite by the accumulative roll bonding process, *J. Mater. Res. Technol.*, 2020, **9**(4), 7880–7886, DOI: **10.1016/j.jmrt.2020.05.084**.

12 Z. Zhang, W. M. Jiang, F. Guan, G. Y. Li and Z. T. Fan, Interface formation and strengthening mechanisms of Al/Mg bimetallic composite via compound casting with rare earth Ce introduction, *Mater. Sci. Eng., A*, 2022, **854**, 143830, DOI: **10.1016/j.msea.2022.143830**.

13 S. Jiang, R. L. Peng, Z. Hegedus, T. Herold, J. J. Moverare, U. Lienert, F. Fang, X. Zhao, L. Zuo and N. Jia, Micromechanical behavior of multilayered Ti/Nb composites processed by accumulative roll bonding: an in-situ synchrotron X-ray diffraction investigation, *Acta Mater.*, 2021, **205**, 116546, DOI: **10.1016/j.actamat.2020.116546**.

14 W. C. Liu, Y. J. Ke, K. Sugio, X. G. Liu, Y. Guo and G. Sasaki, Microstructure and mechanical properties of Al₂O₃-particle-reinforced Al-matrix composite sheets produced by accumulative roll bonding (ARB), *Mater. Sci. Eng., A*, 2022, **850**, 143574, DOI: **10.1016/j.msea.2022.143574**.

15 M. Alizadeh, Processing of Al/B4C composites by cross-roll accumulative roll bonding, *Mater. Lett.*, 2010, **64**(23), 2641–2643, DOI: **10.1016/j.matlet.2010.08.039**.

16 M. Avazzadeh, M. Alizadeh and M. Tayyebi, Structural, mechanical, and corrosion evaluations of Cu/Zn/Al multilayered composites subjected to CARB process, *J. Alloys Compd.*, 2021, **867**, 158973, DOI: **10.1016/j.jallcom.2021.158973**.

17 M. Alizadeh and M. Samiei, Fabrication of nanostructured Al/Cu/Mn metallic multilayer composites by accumulative roll bonding process and investigation of their mechanical properties, *Mater. Des.*, 2014, **56**, 680–684, DOI: **10.1016/j.matdes.2013.11.067**.

18 N. Kalantarrashidi, M. Alizadeh and S. Pashangeh, Consideration on zinc content on the microstructure, mechanical, and corrosion evolution of aluminum/zinc composites fabricated by CARB process, *J. Mater. Res. Technol.*, 2022, **19**, 1805–1820, DOI: **10.1016/j.jmrt.2022.05.133**.

19 L. Chen, Q. N Shi, D. Q. Chen, S. P. Zhou, J. L. Wang and X. M. Luo, Research of textures of ultrafine grains pure copper produced by accumulative roll-bonding, *Mater. Sci. Eng., A*, 2009, **508**(1–2), 37–42, DOI: **10.1016/j.msea.2008.12.018**.

20 D. C. C. Magalhaes, O. M. Cintho, J. B. Rubert, V. L. Sordi and A. M. Kliauga, The role of shear strain during Accumulative Roll-Bonding of multilayered composite sheets: pattern formation, microstructure and texture evolution, *Mater. Sci. Eng., A*, 2020, **796**, 140055, DOI: **10.1016/j.msea.2020.140055**.

21 Q. Su, J. Xu, C. X. Wang, D. B. Shan and B. Guo, The Fabrication of Micro-Array Channels with the Ultrafine-Grained LZ91 Mg–Li Alloy by Micro-Embossing, *Micromachines*, 2018, **9**(2), 55, DOI: **10.3390/mi9020055**.

22 H. Ji, G. H. Wu, W. C. Liu, X. L. Zhang and M. X. Wang, Origin of the age-hardening and age-softening response in Mg–Li–Zn based alloys, *Acta Mater.*, 2022, **226**, 117673, DOI: **10.1016/j.actamat.2022.117673**.

23 L. Z. Liu, X. H. Chen, J. F. Wang, L. Y. Qiao, S. Y. Gao, K. Song, C. Y. Zhao, X. F. Liu, D. Zhao and F. S. Pan, Effects of Y and Zn additions on electrical conductivity and electromagnetic shielding effectiveness of Mg–Y–Zn alloys,

J. Mater. Res. Technol., 2018, **35**(6), 1074–1080, DOI: **10.1016/j.jmst.2018.12.010**.

24 W. Habila, H. Azzeddine, B. Mehdi, K. Tirsatine, T. Baudin, A. L. Helbert, F. Brisset, S. Gautrot, M. H. Mathon and D. Bradai, Investigation of microstructure and texture evolution of a Mg/Al laminated composite elaborated by accumulative roll bonding, *Mater. Charact.*, 2019, **147**, 242–252, DOI: **10.1016/j.matchar.2018.11.010**.

25 A. Macwan, X. Q. Jiang, C. Li and D. L. Chen, Effect of annealing on interface microstructures and tensile properties of rolled Al/Mg/Al tri-layer clad sheets, *Mater. Sci. Eng., A*, 2013, **587**, 334–351, DOI: **10.1016/j.msea.2013.09.002**.

26 Y. Wang, Y. Liao, R. Z. Wu, N. Turakhodjaev, H. T. Chen, J. H. Zhang, M. L. Zhang and S. Mardonakulov, Microstructure and mechanical properties of ultra-lightweight Mg–Li–Al/Al–Li composite produced by accumulative roll bonding at ambient temperature, *Mater. Sci. Eng., A*, 2020, **787**, 139494, DOI: **10.1016/j.msea.2020.139494**.

27 K. Wu, H. Chang, E. Maawad, W. M. Gan, H. G. Brokmeier and M. Y. Zheng, Microstructure and mechanical properties of the Mg/Al laminated composite fabricated by accumulative roll bonding (ARB), *Mater. Sci. Eng., A*, 2010, **527**, 3073–3078, DOI: **10.1016/j.msea.2010.02.001**.

28 D. Rahmatabadi, M. Ahmadi, M. Pahlavani and R. Hashemi, DIC-based experimental study of fracture toughness through R-curve tests in a multi-layered Al–Mg (LZ91) composite fabricated by ARB, *J. Alloys Compd.*, 2021, **883**, 160843, DOI: **10.1016/j.jallcom.2021.160843**.

29 H. Chang, M. Y. Zheng, C. Xu, G. D. Fan, H. G. Brokmeier and K. Wu, Microstructure and mechanical properties of the Mg/Al multilayer fabricated by accumulative roll bonding (ARB) at ambient temperature, *Mater. Sci. Eng., A*, 2012, **543**, 249–256, DOI: **10.1016/j.msea.2012.02.083**.

30 S. Mroz, A. Wierzba, A. Stefanik and P. Szota, Effect of Asymmetric Accumulative Roll-Bonding process on the Microstructure and Strength Evolution of the AA1050/AZ31/AA1050 Multilayered Composite Materials, *Materials*, 2020, **13**(23), 5401, DOI: **10.3390/ma13235401**.